Dalton Transactions

ROYAL SOCIETY OF CHEMISTRY

PAPER

View Article Online
View Journal | View Issue

Cite this: *Dalton Trans.*, 2024, **53**, 14817

Hydrogen evolution driven by heteroatoms of bidentate N-heterocyclic ligands in iron(II) complexes†

Soma Keszei, *[a,b] Yiqing Wang,[c] Haotian Zhou,[c] Tamás Ollár, [b] Éva Kováts,[d] Krisztina Frey,[b] Levente Tapasztó,[a] Shaohua Shen [c] and József Sándor Pap [b]

While Pt is considered the best catalyst for the electrocatalytic hydrogen evolution reaction (HER), it is evident that non-noble metal alternatives must be explored. In this regard, it is well known that the binding sites for non-noble metals play a pivotal role in facilitating efficient catalysis. Herein, we studied Fe(II) complexes with bidentate 2-(2′-pyridyl)benzoxazole ($\mathbf{L^O}$), 2-(2′-pyridyl)benzthiazole ($\mathbf{L^S}$), 2-(2′-pyridyl)benzimidazole ($\mathbf{L^{NH}}$), and 2–2′-bipyridyl ($\mathbf{L^{py}}$) ligands – by adding trifluoroacetic acid (TFA) to their acetonitrile solution – in order to examine how their reactivity towards protons under reductive conditions could be impacted by the non-coordinating heteroatoms (S, O, N, or none). By applying this ligand series, we found that the reduction potentials relevant for HER correlate with ligand basicity in the presence of TFA. Moreover, DFT calculations underlined the importance of charge distribution in the ligand-based LUMO and LUMO+1 orbitals of the complexes, dependent on the heterocycle. Kinetic studies and controlled potential electrolysis – using TFA as a proton source – revealed HER activities for the complexes with $\mathbf{L^{NH}}$, $\mathbf{L^O}$, and $\mathbf{L^S}$ of k_{obs} = 0.03, 1.1, and 10.8 s^{-1} at overpotentials of 0.81, 0.76, and 0.79 V, respectively, and pointed towards a correlation between the kinetics of the reaction and the non-coordinating heteroatoms of the ligands. In particular, the activity was associated with the [Fe($\mathbf{L^{S/O/NH}}$)$_2$(S)$_2$]$^{2+}$ form (S = solvent or substrate molecule), and the rate-determining step involved the formation of [Fe(H–H)]$^+$, during the weakening of Fe–H and CF_3CO_2–H bonds, according to the experimental and DFT results.

Received 19th July 2024,
Accepted 5th August 2024

DOI: 10.1039/d4dt02081b

rsc.li/dalton

Introduction

The utilization of H_2 as a green chemical energy carrier is an attractive possibility; however, only less than 4% of the current H_2 production comes from cheap and green water electrolysis.[1,2] Sustainable production is also important since H_2 is a widely used raw material in the chemical industry.[2,3] Electrocatalytic H_2 production can be a more appealing option only if cheap and efficient catalysts are used. While precious metals are efficient catalysts for the cathodic hydrogen evolution reaction (HER) of water splitting, their price and accessibility will limit their widespread application with time.[4–7]

Several transition metal complexes have been found so far to act as a catalyst for the electrochemical HER.[8–13] These molecular catalysts may present a high specific activity and robustness through several catalytic cycles. A common feature of natural[14] and artificial[8–13] catalysts in this process is that HER proceeds through a number of consecutive or coupled electrochemical and chemical steps.

In most cases, catalytic reactions are proposed to proceed *via* metal–hydride (M–H) intermediates. A general reaction route for HER is shown in Scheme 1.[15,16] The catalytic cycle typically begins with an electron transfer, involving the molecular orbitals of the metal centre, which enables the binding of the substrate and the formation of M–H intermediates. In some cases, a protonation reaction takes place prior to the electron transfer reaction, yielding a hydride intermediate (M–H) (Scheme S1, Tables S1 and 2†). A homolytic reaction mechanism can be assumed if H_2 is formed by a bimetallic reaction of the M–H species in a reductive elimination reaction. In other cases, M–H intermediates are attacked by a second sub-

[a]*Centre for Energy Research, Institute of Technical Physics and Materials Science, H-1121, Konkoly-Thege út 29-33, Budapest, Hungary.*
E-mail: keszei.soma@ek.hun-ren.hu
[b]*Centre for Energy Research, Surface Chemistry and Catalysis Department, H-1121, Konkoly-Thege út 29-33, Budapest, Hungary*
[c]*International Research Center for Renewable Energy (IRCRE), State Key Laboratory of Multiphase Flow in Power Engineering (MFPE), Xi'an Jiaotong University, Xi'an, Shaanxi 710049, China*
[d]*Institute for Solid State Physics and Optics, Wigner Research Centre for Physics, P.O. Box 49, H-1525 Budapest, Hungary*

†Electronic supplementary information (ESI) available. CCDC 2288829. For ESI and crystallographic data in CIF or other electronic format see DOI: https://doi.org/10.1039/d4dt02081b

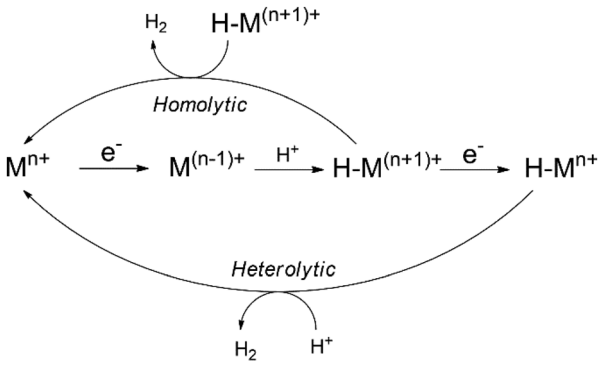

Scheme 1 General mechanism for the HER involving metal–hydride intermediates.[15]

strate (H^+), leading to a heterolytic reaction pathway (Scheme 1).

The reaction mechanism can be also diverse according to the formation of reactive intermediary species (Scheme 2). For a ligand-assisted metal-centred mechanism, the ligands are assumed to play a determinant role in the catalytic cycle through fine-tuning the redox potential and the proton affinity of the metal centre.[16] However, in some cases the direct participation of ligand-based molecular orbitals in the electron and proton transfer reactions is also viable, and this is called a metal-assisted, ligand-centred mechanism or just ligand-centred mechanism (Scheme 2).

The above mechanistic scenarios are determined by the particular metal–ligand combination, and the performance can be further tuned by ligand modification. Cobalt,[10,12] nickel,[9–11] copper,[9,10] and other transition metal compounds[9,10] all have great potential in HER electrocatalysis; yet, iron attracts special attention, as it is the most earth-abundant element among all the transition metals. Moreover, this metal is present in the active centre of hydrogenase enzymes that occur in bacteria, archaea, and some eukaryotes, serving as model for bio-inspired catalysts (Scheme S1†).[14,17]

Several types of iron-containing electrocatalysts have been reported recently. Considering the structural features of the compounds, mechanistic insights into the catalytic reactions would be useful. A bio-inspired complex was reported by Rauchfuss,[18] who highlighted its potential in the application of organoiron HER catalysts (Scheme S1†). In addition to the dithiolate bridging ligands, carbonyl and cyanide terminal ligands are bound to the iron centres in organoiron species, similar to the [FeFe]-H_2ases.[14] Note that several analogous compounds have been synthetized and studied in detail.[19–32] Work on iron complexes with sulfur-rich ligands not only proved that basic ligands can act as a proton shuttle,[33,34] but also that some ligands can act as redox active units beside the metal centre and take part in electron transfer reactions.[16] In addition, iron complexes with porphyrin,[35–37] corrole,[38–40] phenantroline,[41] clathrochelate,[42] and polypyridyl[43–47] ligands were also found to be active catalysts for the HER.

Comparison of the possible mechanisms suggest that the first step of a catalytic cycle may be either protonation or electron transfer (Tables S1 and S2†). Bridging ligands favouring bimetallic iron complexes tend to form μ-hydrido complexes that react further in the presence of acids to cationic species, thus producing H_2.[18] Basic moieties attached to the ligands can improve the catalytic activity by promoting the protonation step.[22] The use of sulfur-rich ligands in mono-metallic complexes leads to a different mechanism. The protonation takes place on the basic sulfur atoms coordinated to iron to form cationic species.[33] Recently, protonation on non-coordinating chalcogens was also observed, specifically in the case of iron(II) complexes with tetrapodal bis(benzimidazole)amino thio- and selenoether ligands.[48]

In the case of polypyridyl ligands, the mechanism is assumed to depend on the basicity of the ligand. Basic phenolate groups in ligands can bind protons.[43–45] However, in cases where the catalyst is equipped with a sulfinate ligand,[43] the catalytic cycle starts with an electron transfer that increases the proton affinity of the metal centre, making the M–H intermediate viable. A similar behaviour, *i.e.* for the first step of the catalysis, involving the reduction of iron, followed by protonation, was observed when catalysts with porphyrin-,[35–37] corrole-,[38,39] and clathrochelate[42]-type ligands were studied.

In this study, we investigated the reactivity of four Fe(II) complexes, each containing bidentate ligands (2-(2′-pyridyl) benzoxazole ($\mathbf{L^O}$), 2-(2′-pyridyl)benzthiazole ($\mathbf{L^S}$), 2-(2′-pyridyl) benzimidazole ($\mathbf{L^{NH}}$), and 2-2′-bipyridyl ($\mathbf{L^{py}}$) (Scheme 3)) towards protons, upon reduction, in order to establish relationships between the chemical properties of the ligands and the reaction rate. These compounds were earlier studied

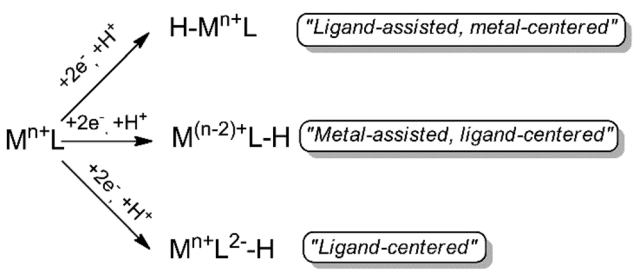

Scheme 2 Proposed molecular mechanisms of the HER catalyzed by transition metal complexes.[16]

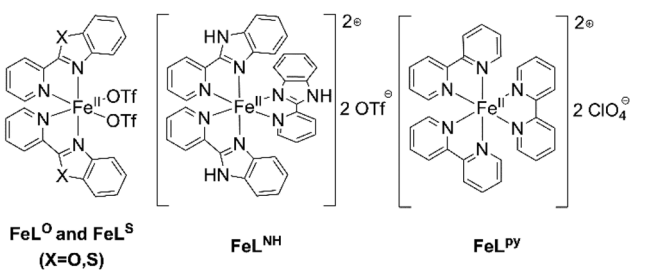

Scheme 3 Structures of the coordination compounds involved in this study.

as functional models of catalase enzymes,[49] or anodic electrocatalysts for oxygen evolution.[50] The results then suggested that the non-coordinating heteroatoms of the $\mathbf{L^{O/S/NH}}$ ligands in Fe(II) pre-catalysts fundamentally determined the activity and stability of the corresponding oxidized species. In the present study, we investigated, if a similar – and not yet demonstrated – effect applies under reductive conditions; that is, either the stability of the reduced complex or the protonated intermediate depends on a non-coordinated heteroatom. As shown by our combined experimental findings and DFT calculations, the non-coordinating heteroatoms fundamentally determine the behaviour of the complexes. The differences in the redox behaviour and reactivity of the compounds showed a trend with the basicity of the ligands and the charge distribution of the LUMO and LUMO+1 orbitals, that in turn depended on the non-coordinating O/S/NH function. However, tunnelling effects appear to be crucial in the reactivity of the complexes.

Experimental

Materials and synthesis

Acetonitrile, trifluoroacetic acid (TFA) and d-TFA (99.5%), tetrabutylammonium perchlorate (TBAP), and ligands 2-(2-pyridyl)benzimidazole ($\mathbf{L^{NH}}$) and 2,2-bipyridyl ($\mathbf{L^{py}}$) were purchased from commercial sources and used without further purification. The ligands 2-(2-pyridyl)benzoxazole ($\mathbf{L^{O}}$) and 2-(2-pyridyl)benzthiazole ($\mathbf{L^{S}}$) were synthesized as per a previously published method.[49]

$[Fe^{II}(L^{NH})_3](OTf)_2$, $[Fe^{II}(L^{O})_2(OTf)_2]$, and $[Fe^{II}(L^{S})_2(OTf)_2]$. The complexes were synthesized according to known procedures to give spectroscopically confirmed crystalline products in similar yields as reported earlier.[49] Anal. calc. for $[Fe^{II}(L^{NH})_3](OTf)_2$: C, 48.57; H, 2.90; N, 13.42; found: C, 47.77; H, 3.09; N, 13.47.

Anal. calc. for $[Fe^{II}(L^{O})_2(OTf)_2]\cdot 3H_2O$: C, 39.01; H, 2.77; N, 7.00; found: C, 38.77; H, 2.31; N, 7.03. Anal. calc. for $[Fe^{II}(L^{S})_2(OTf)_2].H_2O$: C, 39.20; H, 2.28; N, 7.03; found: C, 38.78; H, 2.43; N, 7.03. The structure of $[Fe^{II}(L^{S})_2(OTf)_2]$ was characterized by X-ray crystallography. The red microcrystalline product was recrystallized by layering diethyl-ether on concentrated acetonitrile solution to obtain single crystals. The structures of $[Fe^{II}(L^{NH})_3](ClO_4)_2$ [51] and $[Fe^{II}(L^{O})_2(OTf)_2]$ were published earlier.

$[Fe^{II}(L^{py})_3](ClO_4)_2$. A known procedure was followed,[52] with minor modifications: $FeCl_2$ (0.1 g) was dissolved in a minimum amount of water and $\mathbf{L^{py}}$ (0.4 g) was dissolved in a minimum amount of ethanol. The two solutions were then mixed and $NaClO_4$ (0.2 g), dissolved in water, was added. The resulting deep red precipitate was filtered off, and then washed with cold water and finally with cold ethanol. The product was recrystallized from acetonitrile. Yield: 71.8%. Anal. calc. for $[Fe^{II}(L^{py})_3](ClO_4)_2$: C, 49.82; H, 3.34; N, 11.62; found: C, 49.74; H, 3.42; N, 11.72.

Electrochemistry. Cyclic voltammetry (CV) and square wave voltammetry (SWV) experiments were performed using a BioLogic SP-150 galvano/potentiostat with a conventional three-electrode configuration, consisting of a glassy carbon (GC) working electrode (ID = 3 mm, polished before the experiments), a Pt auxiliary electrode, and Ag/Ag^+ reference electrode (0.01 M $AgNO_3$, 0.1 M TBAP/MeCN). The potentials are given against the ferrocenium/ferrocene (Fc^+/Fc) couple measured in the same cell, under the same conditions. The solutions were bubbled with argon to ensure an inert atmosphere during the measurements. Parameters for SWV: PW = 60 ms (f = 8.3 Hz, PH = 32 mV, SH = −4 mV).

Controlled potential electrolysis (CPE) experiments were performed in a screw mount electrochemical H-cell (2 × 15 ml), purchased from redoxme AB with a conventional three-electrode configuration, consisting of a GC working electrode (ID = 6 mm, polished before each experiment, except for the rinse tests), a Pt auxiliary electrode, and Ag/Ag^+ pseudo-reference electrode (0.1 M TBAP/MeCN). The potentials were referenced and plotted against the Fc^+/Fc couple. All the solutions were bubbled with argon.

Electrolytic conductivity was determined using a calibrated Consort C533 multi-parameter analyzer.

Gas analysis. The evolution of H_2 was followed by gas chromatography (GC) using a Shimadzu GC 2010 Tracera instrument equipped with a BID detector. Gas samples (V = 100 μL) were taken from the headspace of the cathode compartment of the air-tight H-cell, and injected through an injector unit into a circulation loop (filled with 6.0 He) connected to the sampler. A circulating micro-pump was responsible for homogenization before the sample was injected through the inlet valve. The carrier and the plasma gas were 6.0 He. Calibration for assuring the sample volume and component sensitivity was done with Ar (5% H_2). The instrument settings were as follows: 20 mL min^{-1} total, 50 mL min^{-1} DCG, 3 mL min^{-1} purge flow rate, $T_{col.}$ = 35 °C, $T_{det.}$ = 200 °C.

UV/Vis measurements. UV/Vis titration experiments were carried out using an Agilent Cary 60 spectrophotometer. Aliquots of the solutions (free ligand in section "*Solution chemistry of the complexes*" and TFA in "*Addition of trifluoroacetic acid to the complexes in acetonitrile*") in acetonitrile were added to the solution of the complexes in quartz cuvettes at 25 °C and the solutions were stirred with a magnetic stirrer.

X-Ray diffraction. Single crystals suitable for X-ray diffraction analysis were obtained by layering diethyl-ether on the concentrated acetonitrile solution of $\mathbf{FeL^{S}}$. Single-crystal X-ray diffraction measurements of the typically 100 μm-sized red plate crystals were performed on an Agilent Supernova diffractometer equipped with a dual microfocus source, kappa goniometer, position sensitive detector, and dry nitrogen gas flow cooler. Data were taken at 100 K using the Cu source up to 0.8 Å resolution. The data collection was controlled with CrysAlis[53] software, while the structure solution and refinement were done with SHELX[54] software.

DFT methods. First-principles density functional theory (DFT) calculations were performed using the CASTEP code.[55]

Molecules were placed in a 40 × 40 × 40 cell to shield the effects of periodicity on the molecular calculations. The exchange–correlation effects were treated with the generalized gradient approximation (GGA) with the Perdew–Burke–Ernzerhof (PBE) potential.[56] The interaction between the ionic core and valence electrons was simulated by the ultrasoft pseudopotentials.[57] van der Waals interaction was considered by using the empirical correction in TS (Tkatchenko and Scheffler).[58] The kinetic energy cut-off was chosen as 500 eV. Brillouin zone integration was sampled with 1 × 1 × 1 and 1 × 1 × 1 Monkhorst–Pack mesh *k*-points for the reaction coordinate and the LUMO, LUMO+1 calculations. An implicit solvent model was used to consider the effect of the acetonitrile solvent on the reaction. The structures were allowed to fully relaxed and were optimized until convergence to 10^{-5} eV in total energy and 0.01 eV $Å^{-1}$ in the forces.

Results and discussion

Structural features of the complexes and the crystal structure of $[Fe^{II}(L^{S})_2(OTf)_2]$

In this work, we investigated the Fe(II) complexes of L^{NH}, L^{O}, L^{S}, and L^{py}, (collectively NN′ ligands herein), as shown in Scheme 3. The non-symmetrical NN′ ligands readily reacted with Fe(II) triflate in dry acetonitrile under an inert atmosphere to give solid products upon crystallization. The isolated substance in the case of L^{NH} was the air-stable, red tris-chelate complex, while for $L^{O/S}$, the isolated forms were the orange $[Fe^{II}(L^{O/S})_2(OTf)_2]$ complexes.

The single-crystal structure of $[Fe^{II}(L^{S})_2(OTf)_2]$ is shown in Fig. 1 (for details see Table S3†). The FeN bond distances of *ca.* 2.13–2.20 Å were similar to those determined for **FeL^{O}** (*ca.* 2.15 Å) earlier[49] and characteristic of high-spin Fe complexes.[59] According to the single-crystal structures, $[Fe^{II}(L^{O})_2(OTf)_2]$ and $[Fe^{II}(L^{S})_2(OTf)_2]$ were structural homologs. Both weakly coordinated OTf^- ions were found in the *trans* position to a pyridinic N donor group and the benzo-heterocyclic N donor groups were found *trans* to each other, resulting in an *OC-6-33* ligand configuration. However, in the case of **FeL^{S}**, the structure was disordered (Fig. S1, and Table S4†) and a second isomer with the *OC-6-23* configuration was present with 16.1% occupancy (several single crystals were analyzed giving the same results).

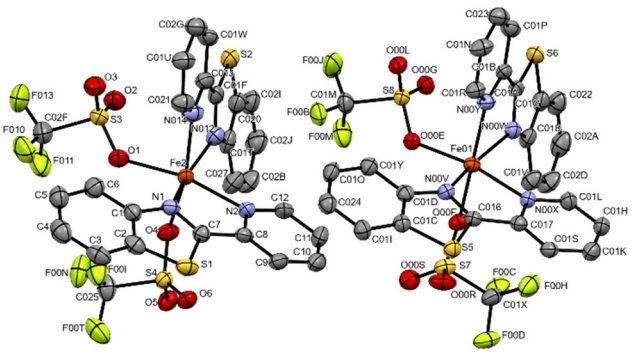

Fig. 1 Crystal structure of $[Fe^{II}(L^{S})_2(OTf)_2]$ (CCDC 2288829†). Ellipsoids are plotted at a 50% probability level. The asymmetric unit consists of two complex molecules differing in the orientation of the triflate anions. Here, the major positional isomer exhibiting the *OC-6-33* configuration with an 83.9% occupancy is shown, while the *minor OC-6-23* isomer (Fig. S1†) and hydrogen atoms are omitted for clarity.

In contrast, $[Fe^{II}(L^{NH})_3](OTf)_2$ exhibited shorter FeN bonds (1.98–2.00 Å), typical for the low-spin state. Note that L^{NH} has been studied in $[Fe(L^{NH})_3]^{2+}$ with ClO_4^-, NO_3^-, I^-, or $B(C_6H_6)_4^-$ counter ions,[60] and moreover, in $[Fe^{II}(L^{NH})_2(SCN)_2]$.[61] The crystal structure of $[Fe^{II}(L^{py})_3]^{2+}$ (abbreviated as **FeL^{py}** herein) with ClO_4^- was reported earlier,[62] showing FeN bond distances close to 1.98 Å.

Solution chemistry of the complexes

The behaviour of the complexes was investigated by several methods in solution. Before the detailed results, a brief is provided for clarity. When dissolved in a coordinating solvent, $[Fe^{II}(L^{NH})_3](OTf)_2$ or $[Fe^{II}(L^{O/S})_2(OTf)_2]$ forms are in part transformed to $[Fe^{II}(L^{S/O/NH})_2(S)_2]^{2+}$ *via* a ligand exchange equilibrium (S stands for solvent molecules; the solution equilibrium systems are referred to as **FeL$^{S/O/NH}$** herein, for acetonitrile).[49,50] **FeL^{py}** is associated with $[Fe^{II}(L^{py})_3](ClO_4)_2$ and $[Fe^{II}(L^{py})_3]^{2+}$ remains the predominant equilibrium species. According to previous studies, **FeL^{S}** and **FeL^{O}** are predominated by the bis-chelate forms, while **FeL^{NH}** and **FeL^{py}** are relatively inert tris-chelates in a dry acetonitrile solution, except for strongly oxidative conditions.[49,50] For example, the homoleptic complex $[Fe^{II}(L^{NH})_3]^{2+}$ and analogues were found to be reactive towards H_2O_2 and organic substrates.[63–67] Thus, a complex, despite the predominance of $[Fe(NN')_3]^{2+}$, remains capable of functioning as a pre-catalyst and exhibiting non-hem oxygenase-like reactivity by partial ligand dissociation. However, no such reactivity has been discussed earlier under reductive conditions.

First, the ionic nature of the dissolved complexes was investigated by their conductivity. Electrolytic conductivity measurements in acetonitrile gave Λ_M values of 278, 258, 275, and 312 Ω^{-1} cm^2 mol^{-1} for **FeL^{NH}**, **FeL^{O}**, **FeL^{S}**, and **FeL^{py}**, respectively (*ca.* 1 mM, at 25 °C). These molar conductivities were consistent with 2 : 1 electrolytes,[68] as could be expected for the $[Fe^{II}(NN')_3]^{2+}$ and $[Fe^{II}(NN')_2(S)_2]^{2+}$ forms. Since the Λ_M values showed the full dissociation of the triflate anions in each case, the solution equilibrium systems were simplified to the $[Fe^{II}(NN')_3]^{2+}$ and $[Fe^{II}(NN')_2(S)_2]^{2+}$ forms in acetonitrile.

Cyclic voltammograms of complexes **FeL$^{S/O/NH/py}$** were recorded in acetonitrile, under an inert atmosphere (Fig. S2†), leading to similar results as previously reported,[49,50] revealing irreversible anodic processes at potentials above −0.5 V *vs.* Fc^+/Fc for **FeL$^{S/O}$**, which were assigned to Fe^{III}/Fe^{II} transitions of the different solution equilibrium species formed upon ligand exchange and oxidation (note that trace water in acetonitrile also participates in anodic equilibria, as was discussed in an earlier work[49]). In the case of **FeL$^{NH/py}$**, a quasi-reversible redox process could be identified ($E_{1/2}$ = 0.52 and 0.7 V *vs.* Fc^+/Fc for

FeL^{NH} and **FeL^{py}**, respectively), indicating its enhanced stability compared to the other compounds. However, in our work we focused on the cathodic processes.

Cathodic polarization leads to irreversible reductions for **FeL$^{S/O/NH}$** below the potential of −1 V *vs.* Fc^+/Fc, indicating reduction processes related to different solution equilibrium species (CE mechanism). Note that no such process could be detected for **FeL^{py}** in the potential range studied; however, two quasi-reversible processes could be observed at −1.7 and −1.88 V *vs.* Fc^+/Fc, which were assigned to ligand-centred reductions, suggesting again the enhanced stability of **FeL^{py}**, compared to the other iron complexes. The CVs of **FeL^{S}** and **FeL^{O}** further showed quasi-reversible redox transitions below −2 V (−2.18 and −2.28 V *vs.* Fc^+/Fc, for **FeL^{S}** and **FeL^{O}**, respectively). These peaks were attributed to ligand reductions.

To get a better insight in to the nature of the reductions, square wave voltammograms (SWVs) of the ligands **L^{S}**, **L^{O}**, **L^{NH}**, and **L^{py}**, and the corresponding complexes were recorded in acetonitrile (Fig. 2, where the numbers stand for the potential values). The ligands exhibited single reduction peaks beyond −2.0 V *vs.* Fc^+/Fc (Fig. 2a) in the order of **L^{S}** > **L^{NH}** > **L^{O}** ≫ **L^{py}** with respect to the potential values. The peaks could be associated with the generation of a $L^{\bullet-}$ radical anion, in which the reducing electron is accepted by the π-antibonding LUMO orbital.[69,70] This process is a quasi-reversible redox transition in the case of **L^{S}** and **L^{O}**, but irreversible in the case of **L^{NH}** in accordance with the ligand-based assignment of the reductions detected by CV experiments (Fig. S2†).

In the SWVs of the complexes, consecutive reductions occurred (Fig. 2b). Based on the reducibility of the free ligands, an obvious assignment for **FeL$^{S/O/NH}$** reductions was that of the ligands coordinated to iron.

This assignment was supported by DFT calculations on the $[Fe^{II}(NN')_2(CH_3CN)_2]^{2+}$ forms of **FeL$^{S/O/NH}$**, suggesting a ligand-based π-antibonding character for the electron-accepting LUMO and LUMO+1 orbitals (Fig. 3). However, the number of current peaks and the ratio between the peak currents were

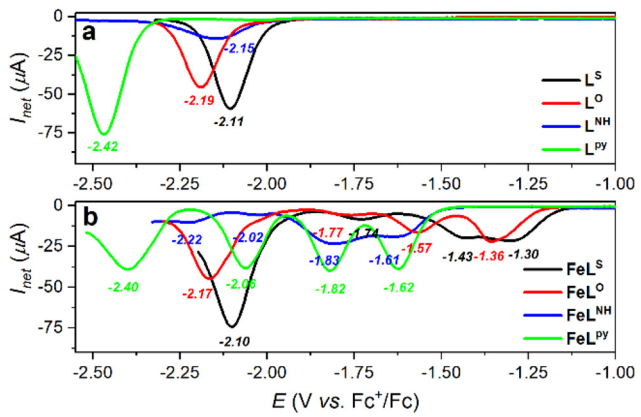

Fig. 2 (a) SWVs of the ligands **L^{S}**, **L^{O}**, **L^{NH}**, and **L^{py}** (1 mM in acetonitrile), and (b) complexes **FeL^{S}**, **FeL^{O}**, **FeL^{NH}**, and **FeL^{py}**.

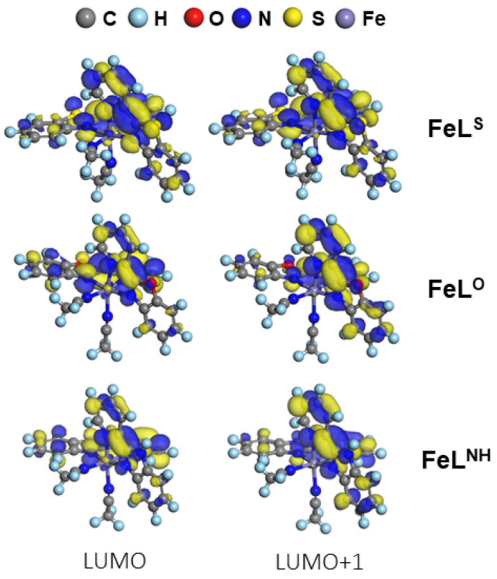

Fig. 3 DFT-calculated LUMO and LUMO+1 orbitals for the $[Fe^{II}(L^{S/O/NH})_2(CH_3CN)_2]^{2+}$ complex forms that have relevance in hydrogen production.

indicative of solution equilibria; therefore, we performed titrations by adding free ligands to the complex solutions.

Upon the titration of **FeL^{S}**, or **FeL^{O}** with the corresponding ligand (**L^{S}** or **L^{O}**), the first reduction peak at −1.30 and −1.36 V *vs.* Fc^+/Fc for **FeL^{S}** and **FeL^{O}**, respectively, underwent an anodic shift (Fig. 4a and b). In contrast, the next peak at −1.43 and −1.57 V *vs.* Fc^+/Fc for **FeL^{S}** and **FeL^{O}**, respectively, was shifted slightly to the cathodic direction. Finally, the intensity of the third peak was enhanced at −1.74 and −1.77 V *vs.* Fc^+/Fc for **FeL^{S}** and **FeL^{O}**, respectively (Fig. 4a and b). In the case of **FeL^{NH}**, an anodic shift of the peaks at −1.83 and −1.61 V *vs.* Fc^+/Fc was also observed with only marginal changes in the intensities (Fig. 4c). Note that the potential range beyond −2.0 V was dominated by excess ligand reduction, and therefore could not be evaluated.

The UV/Vis spectra recorded during the titrations of **FeL^{S}** and **FeL^{O}** (Fig. 4d and e) showed the appearance of bands in the 400–600 nm range – MLCT bands of the tris-chelate complexes[49] – because of the excess ligand in the solutions. In contrast, the MLCT bands were already visible in the case of **FeL^{NH}**, prior to the addition of **L^{NH}** (Fig. 4f), and only a slight increase in the absorbance could be observed during the titration, indicating the predominance of $[Fe(L^{NH})_3]^{2+}$ in dry acetonitrile devoid of TFA. Note, that the spectral range below 350 nm was omitted for clarity, as it was dominated by the bands of the excess ligand.

The combined results from the SWV and UV/Vis titration experiments were in agreement with a ligand dissociation, as shown in Scheme 4, where K_{eq} is the equilibrium constant. According to the differences observed, the equilibrium could be described by a lower value of K_{eq} in the case of **FeL^{NH}** relative to **FeL^{S}** and **FeL^{O}**, indicating a low proportion of $[Fe^{II}(L^{NH})_2(CH_3CN)_2]^{2+}$ species in dry acetonitrile, compared to

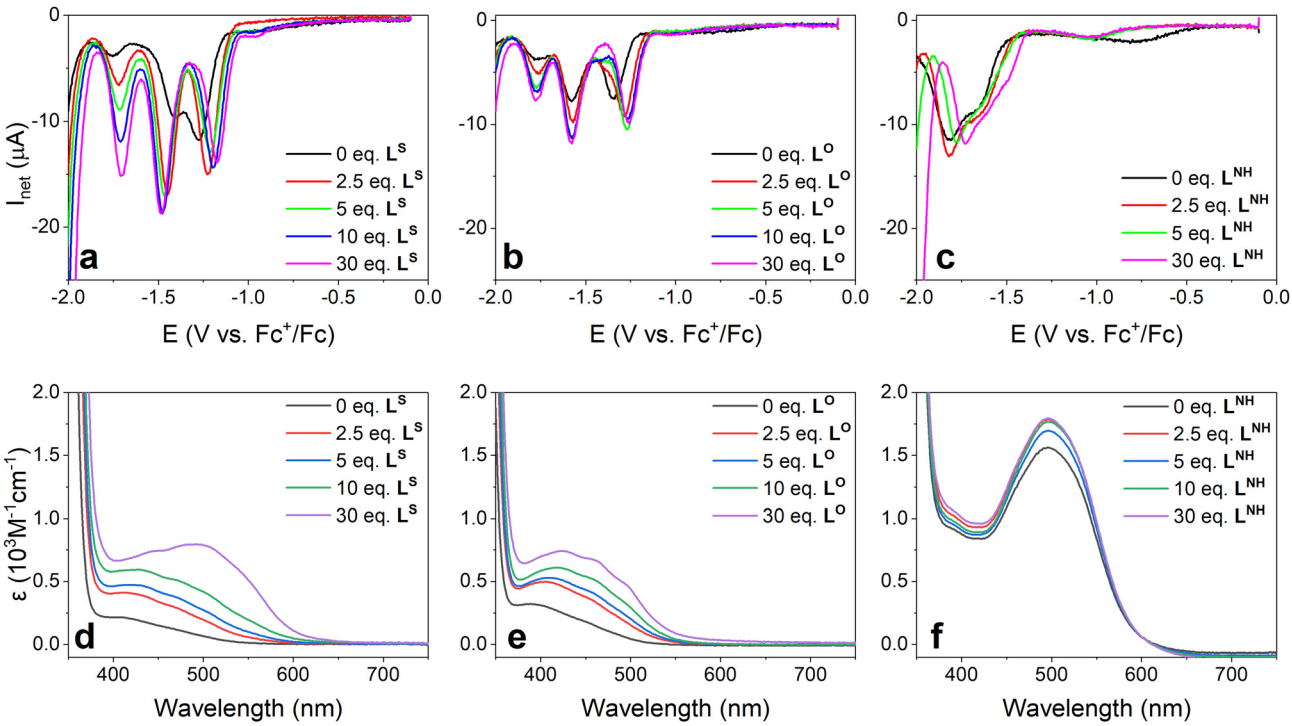

Fig. 4 (a–c) Changes in the square wave voltammograms (0.5 mM in acetonitrile) and (d–f) UV/Vis spectra (0.17 mM in acetonitrile) of complexes FeL^S, FeL^O, and FeL^{NH}, respectively, upon addition of the corresponding ligands L^S, L^O, and L^{NH}.

$$[Fe(NN')_3]^{2+} + 2S \underset{}{\overset{K_{eq}}{\rightleftharpoons}} [Fe(NN')_2(S)_2]^{2+} + NN'$$

NN' = L^S, L^O, L^{NH} or L^{py}
S = solvent

Scheme 4 Ligand dissociation equilibrium; the colour code indicates the predominant equilibrium form in solution.

FeL^S and FeL^O. The equilibrium also allowed assigning the two reduction steps for FeL^S and FeL^O at less negative potential values (Fig. 4a and b, black SWVs, no added $L^{S/O}$) to the LUMO and the energetically close-lying LUMO+1 orbitals of the coordinated ligand in $[Fe^{II}(L^{S/O})_2(CH_3CN)_2]^{2+}$ (Fig. 3).

Note that the conductivities and relevant literature on acetonitrile- and triflate-coordinated Fe(II) complexes[71] rule out the anion-coordinated complex. The third reduction may involve another ligand-based orbital of the tris-chelate form; however – as shown below – it has no relevance in proton reduction.

Addition of trifluoroacetic acid to the complexes in acetonitrile

The addition of 25 equivalents of TFA to FeL^S, FeL^O, or FeL^{NH} in acetonitrile led to new reductions at potentials of −0.86, −0.95, and −1.10 V *vs.* Fc$^+$/Fc, respectively (Fig. 5a). These new peaks were associated with the reduction of the protonated ligand in $[Fe^{II}(NN')(NN'H)(S)_2]^{3+}$. Note that the free ligands behaved in a similar way in the presence of TFA, where the reductions occurred at −0.84, −0.81, and −1.09 V *vs.* Fc$^+$/Fc, for L^S, L^O, and L^{NH}, respectively (Fig. 5b). Importantly, a peak at −1.02 V *vs.* Fc$^+$/Fc appeared in the SWV of L^{py} upon the addition of TFA (Fig. 5b), but no new redox event could be observed in the case of FeL^{py} (Fig. 5a). Therefore, in the case of FeL^{py}, the protonated complex was not formed, in contrast to the corresponding protonation of FeL^S, FeL^O, and FeL^{NH}. This conclusion was also supported by the UV/Vis titration experiments, which showed no protonation reaction in the case of FeL^{py} (*vide infra*).

The reduction potentials of FeL^S, FeL^O, and FeL^{NH} with excess TFA followed the trend for the pK_a values for the heterocyclic ligands (Table 1), representing the 2-H acidity and thereby a trend in the stability of the ligands.[72] The correlation between the pK_a values and reduction peak potentials suggested again that the electron transfer involved the protonated ligand.

Protonated imidazole derivatives, like $L^{NH}H^+$, are known for their increased stability, due to having a symmetrical structure. This is consistent with the highest observed cathodic potential among the complexes that was needed to reduce $FeL^{NH}H^+$. The differences between FeL^SH^+ and FeL^OH^+ can be explained by the tendency of the S and O heteroatoms to contribute to the aromatic ligand π orbitals according to the involved 2p *vs.* 3p orbital, respectively. These electronic effects also explain the minor equilibrium proportion of the tris-complexes in the case of FeL^S and FeL^O, compared to FeL^{NH}.

The addition of various acids (acetic, benzoic, and salicylic acid) to the acetonitrile solution of FeL^S resulted in significant shifts of the E_p potentials (Fig. S3†). The peak potentials

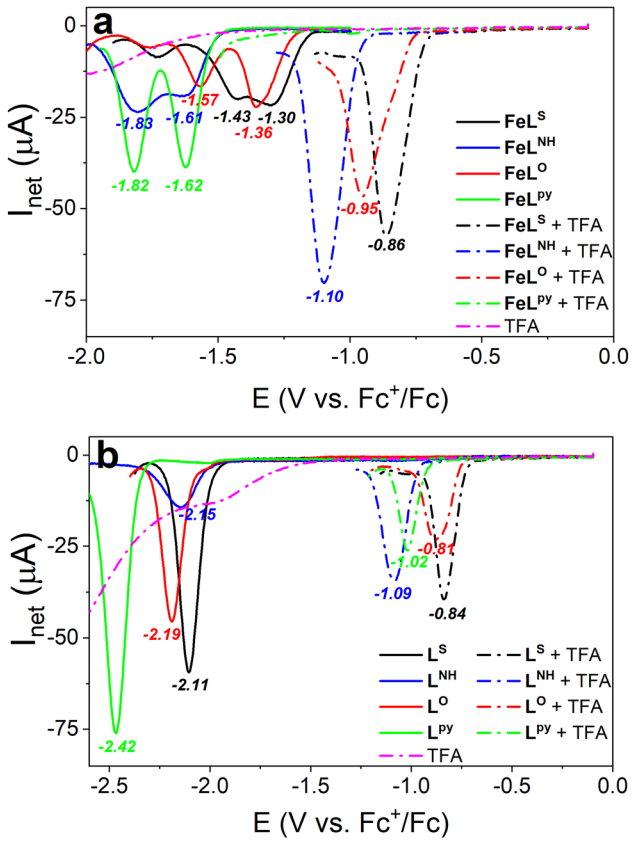

Fig. 5 SWVs (1 mM in acetonitrile) of (a) complexes FeL^S, FeL^O, FeL^{NH}, and FeL^{py} and (b) ligands L^S, L^O, L^{NH}, and L^{py} in the presence or absence of 25 mM TFA.

Table 1 pK_a of the aryl moieties (Ar) in the 2-position of pyridine in L^S, L^O, and L^{NH} and the reduction potentials for the complexes in the presence of TFA (Fig. 5a)

	pK_a(Ar)[a]	E_p[b]
FeL^{NH}	16.4	−1.10
FeL^O	24.4	−0.95
FeL^S	27	−0.86

[a] Measured in DMSO.[72] [b] V *vs.* Fc^+/Fc for FeL^S, FeL^O, and FeL^{NH}.

exhibited a correlation with the pK_a values of the acids used,[73] further supporting the notion that this reduction event can be assigned to FeL^SH^+.

In the UV/Vis spectra of FeL^S, FeL^O, FeL^{NH}, and FeL^{py} in acetonitrile, intense intra-ligand charge transfer (ILCT) bands could be observed between 220 and 330 nm (Fig. S4†), originating from π–π* transitions.[50] In the case of FeL^S, FeL^O, and FeL^{NH}, the MLCT bands were partly hindered by the strong ILCT bands near 300 nm, but these bands could be clearly seen in the absorption spectrum of FeL^{py} at 350 and 392 nm. Other MLCT bands at 486 and 527 nm – typical for Fe(II) complexes[49] – were also pronounced in the spectrum of FeL^{py}, in accordance with the predominant $[Fe(L^{py})_3]^{2+}$ form.

Upon the addition of TFA, the intensity of the ILCT bands for FeL^S and FeL^O decreased roughly at 300 nm and simultaneously, new bands appeared at higher wavelengths (Fig. 6a, b, and Fig. S4†). The slight shift in isosbestic points suggested more than two absorbing species, thus a coupled protonation-ligand exchange process is assumed (Scheme 5). The titration of FeL^{NH} revealed a different, hypsochromic shift in the absorption bands (Fig. 6c and Fig. S4†). The origin of this behaviour is unclear, but the presence of a third L^{NH} dissociating from the $[Fe(L^{NH})_3]^{2+}$ can be assumed responsible (Scheme 5). The coordinated heterocyclic ligand L^{NH} – although capable of undergoing protonation – is replaced by weakly coordinating monodentate ligands that may lead to a more complex equilibrium system (note that FeL^{NH} showed a very low proton reduction ability *a priori* that turned our attention rather to FeL^S and FeL^O).

In contrast, the titration of FeL^{py} with TFA was ineffective with respect to the ILCT band (Fig. 6d and Fig. S4†). The dominance of the six-coordinated tris-complex explains this behaviour. The findings on FeL^{py} further support a ligand exchange coupled to NN′ ligand protonation for FeL^S and FeL^O.

Enhanced Faraday current with TFA added to the complex solutions

The addition of TFA in high excess (250 equivalents) to FeL^O, FeL^S, FeL^{NH}, or FeL^{py} resulted an enhanced cathodic current – related to the reduction of protons to H_2 – beyond −1.2 V *vs.* Fc^+/Fc (Fig. 7 and Fig. S5†), compared to that of a pure TFA solution (Fig. 7, black CV). Note, that no considerable current enhancement could be observed in the CV of the free ligands in the presence of TFA (Fig. S6†). TFA is widely used as a proton source in electrochemical HER studies as it shows less interference from background current than other acids.[10] Owing to the weak coordination ability of trifluoroacetic anion, a significant effect on the solution chemical equilibria could be also ruled out. The enhanced reduction occurred at a considerably higher cathodic potential than the first reduction of the coordinated ligand (Fig. 5a and 7), and was characterized by increasing overpotential in the order of FeL^O, FeL^S, and FeL^{NH} (Table 2).

Controlled potential electrolysis (CPE) in acetonitrile followed by gas chromatography (GC) analysis of the headspace gas revealed hydrogen production. The applied potential (−1.48 *vs.* Fc^+/Fc) was selected to minimize the effect of electrode fouling by TFA (Fig. S7†).[73]

Hydrogen could be detected by GC for all the complexes together with a high Faraday efficiency (FE, Table 3), where the reactivity of FeL^S proved to be superior compared to the other complexes, producing hydrogen with an FE of 86.4% and TON of 2.8 after 100 min, as detected by GC (Fig. S8–S10† and Table 3). FeL^O, FeL^{NH}, and FeL^{py} showed poor performance, and their TON values did not even reach 1 after 1 h of reaction time (Fig. S10†). In the case of FeL^{py}, a surface deposit could be also observed on the surface of the glassy carbon electrode after the experiment.

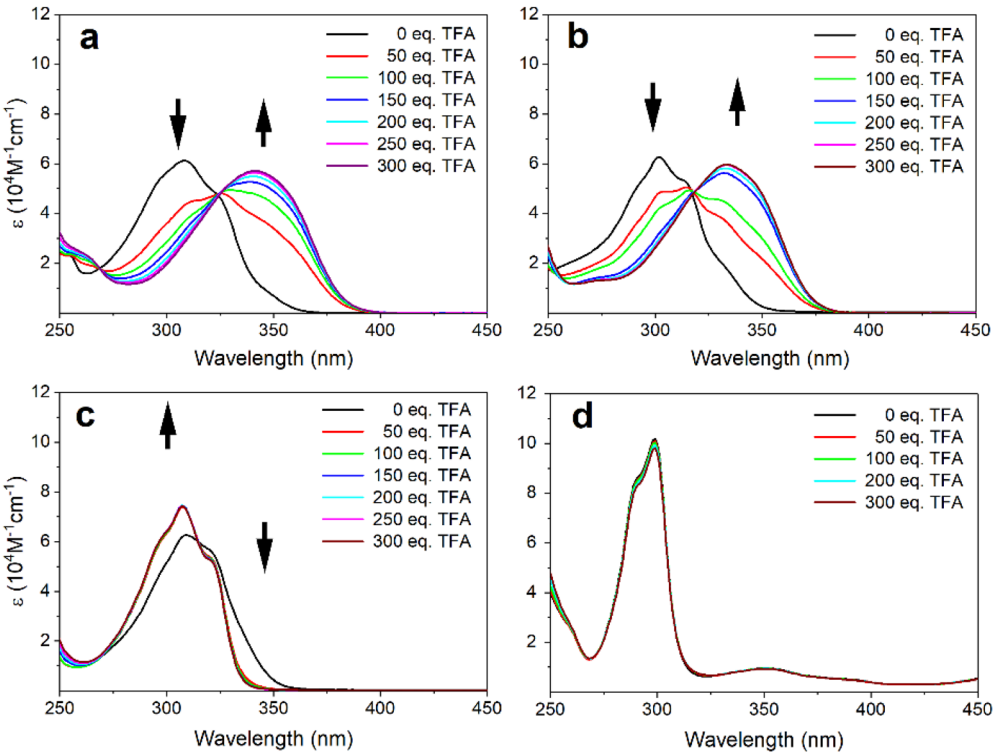

Fig. 6 UV/Vis titration experimental results for complexes (a) FeL^{S}, (b) FeL^{O}, (c) FeL^{NH}, and (d) FeL^{py} (0.01 mM, in acetonitrile).

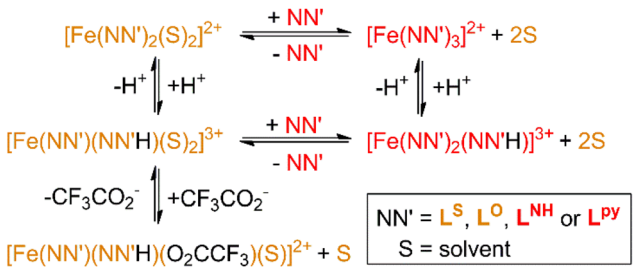

Scheme 5 Proposed protonation and ligand exchange reactions for complexes FeL^{S}, FeL^{O}, FeL^{NH}, and FeL^{py} (colour code indicates the predominant species).

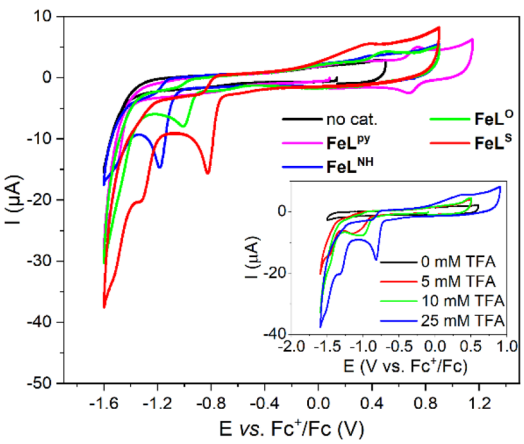

Fig. 7 Difference in the CV of 25 mM TFA in acetonitrile in the absence and in the presence of each complex (0.1 mM); inset: changes in the CV of FeL^{S} (0.1 mM in acetonitrile) as a result of the increasing TFA concentration.

It must be mentioned that some disturbing effects, such as electrode fouling by TFA and the electrochemical reduction of the residual oxygen in the cell, could not be fully excluded, but were taken into consideration by a background correction of the passed charge.

Following CPE, the electrodes were gently washed with acetone and acetonitrile, and the experiments were repeated to check for any active deposits on the GC electrode (Fig. S11†). For each of the complexes, only an insignificant amount of hydrogen could be detected in the headspace of the cell using the rinsed electrode in pure TFA solution. However, in the case of FeL^{O}, even less hydrogen was produced in the rinse test than during the background experiment (Fig. S11, and S12†). The reason for this must be that there was an insulating surface layer on the glassy carbon working electrode from the complex. Note that the surface deposit formed *in situ* from FeL^{py} did not yield hydrogen in a follow-up experiment.

Altogether, it could be noted that only a low catalytic activity could be observed for the best complex (FeL^{S}) and almost no activity at all for the worst performing complex (FeL^{py}). However, the structural resemblance of the four compounds make it possible to better understand the mechanism of the reaction and allow us to draw conclusions about the role

Table 2 Summary of electrochemical proton reduction of $\mathbf{FeL^S}$, $\mathbf{FeL^O}$, and $\mathbf{FeL^{NH}}$ (0.1 mM in acetonitrile with 25 mM TFA)

	Onset potential (V *vs.* Fc^+/Fc)[a]	η[b] (V)	k_{obs}[c] (s^{-1})	k_{DFT}[d] (s^{-1})
$\mathbf{FeL^{NH}}$	−1.49	0.81	0.03	0.05
$\mathbf{FeL^O}$	−1.44	0.76	1.1	1.6
$\mathbf{FeL^S}$	−1.47	0.79	10.8	16.45

[a] Onset potentials (E_{onset}) were determined by the first derivative method.[74] [b] Overpotential (η) = E_{onset} − $E(H^+/H_2)$;[74] $E(H^+/H_2)$ = 0.68 V *vs.* Fc^+/Fc.[75] [c] Experimental value based on eqn (2). [d] Theoretical value based on DFT calculations (see below).

Table 3 Results of the controlled potential electrolysis experiments

	FE[a] (%)	TON[b]
$\mathbf{FeL^S}$	86.4	1.70
$\mathbf{FeL^O}$	97.4	0.36
$\mathbf{FeL^{NH}}$	93.1	0.28
$\mathbf{FeL^{py}}$	93.7	0.19

[a] Background corrected. [b] After 60 min.

of the non-coordinating heteroatoms in the ligand series. In this regard, our attention was turned towards the deeper understanding of the reaction mechanism, in order to observe the structure–activity relationships through the different reactivities of the studied complexes.

Upon increasing the concentration of TFA by a constant complex concentration, a proportional increase in the excess cathodic currents (i_c) could be observed (Fig. 7, inset; Fig. S5†). The linear relationship between i_c and [TFA] suggested a second-order dependence on the proton concentration (Fig. S13a†). Since i_c was also correlated with the complex concentrations, *i.e.* [c] (Fig. S13b†), altogether the following expression can be used to describe the reaction rate (eqn (1)):

$$v = k[c][H^+]^2 \quad (1)$$

Note that in the case of $\mathbf{FeL^{py}}$, only a modest current enhancement occurred that increased from cycle to cycle, and visible traces of a deposited ad-layer on the working electrode could be observed (Fig. S14†), making the evaluation of the molecular activity unreasonable.

Next, pseudo-first-order conditions were set by the addition of 250 equivalents of TFA, which allowed us to calculate a k_{obs} value for each complex (Table 2, and Fig. S15†) by the following expression[10] (eqn (2)):

$$\frac{i_c}{i_p} = \frac{n}{0.4463}\sqrt{\frac{RTk_{obs}}{F\nu}}, \quad (2)$$

where i_c represents the excess cathodic current, measured at the onset potentials as defined in Table 2; i_p represents the preceding one-electron reduction peak current; n is the number of electrons involved (2); R is the molar gas constant (8.314 J mol^{-1} K^{-1}); T is the temperature (298 K); F is the Faraday constant (96 485 C mol^{-1}); and ν is the scan rate (V s^{-1}). Note, that this expression is generally used for an ideal electrocatalytic plateau response under pure kinetic conditions; however, it can be also used for more complicated systems for the purpose comparing catalysts. Nevertheless, it must be taken into consideration that the resulting k_{obs} value will be underestimated in such cases.[10,76] Here, the onset potentials were determined by the inflexion points and confirmed by the first derivatives of the polarization curves (Fig. S16†).[74] The inflexion point refers to the potential region where the electron-transfer rate is a maximum. At greater potentials, the reaction is limited by the diffusion of substrate molecules to the electrode surface.[74,76,77] Since no redox events could be detected at the potential region of the hydrogen evolving reaction prior to the addition of the acid, the first step of the reaction has to be the protonation of the complex, and the protonated species are the actual active compounds. For the same reason, i_p in eqn (2) was approximated by the peak current of the first reduction event assigned to the protonated ligands (Fig. 5a and 7).

Our data indicate that $\mathbf{FeL^S}$ had the highest reactivity, followed by $\mathbf{FeL^O}$; moreover, $\mathbf{FeL^{NH}}$ performed very poorly in proton reduction. The order in reactivity based on the kinetic analysis of the CVs was in good agreement with hydrogen quantification based on the CPE experiments.

Proposed mechanism for hydrogen evolution by the $\mathbf{FeL^{S/O/NH}}$ system

The proposed general mechanism for hydrogen evolution – based on the combined experimental results and DFT calculations – is summarized in Scheme 6 for the different NN′ complexes. As discussed, the reactive form is $[Fe^{II}(NN')_2(S)_2]^{2+}$ (S = CH_3CN). The first, one-electron reduction of the complexes in the presence of TFA was characterized with the E_p potential values (Table 1), showing a good correlation with the NN′

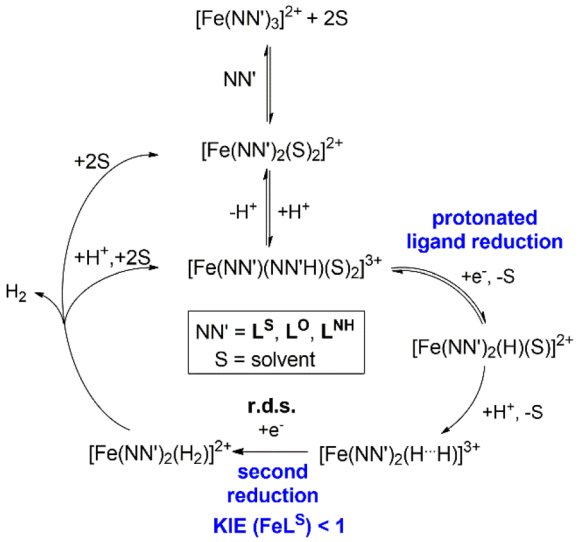

Scheme 6 Proposed mechanism for the hydrogen evolution.

ligand basicity in the order of $\mathbf{FeL^S}$ > $\mathbf{FeL^O}$ > $\mathbf{FeL^N}$. This reduction was assigned to $[Fe^{II}(NN')(NN'H)(S)_2]^{3+}$, and did not induce the reaction by itself. The ligand protonation can serve as a proton shuttle to the reaction centre in this singly reduced state, where it can be attacked by a second proton, similarly to what occurs for known iron-based electrocatalysts.[16] The trends in the reduction potentials, the pK_a values (Table 1), and the calculated free energy changes for the protonation reaction that was assumed to be the pre-equilibrium step of the hydrogen producing cycle ($\mathbf{FeL^S}$ > $\mathbf{FeL^O}$ > $\mathbf{FeL^{NH}}$, Table S5,† and Scheme 6) were all in agreement.

Note that the protonation reaction was found to be more likely to happen on the coordinating N atoms of the ligands, as structures with the proton attached to the non-coordinating heteroatoms resulted in higher energies for the DFT-optimized geometries.

The onset of hydrogen evolution is triggered by a second reduction step at more negative potentials that is also dependent on the ligand (Scheme 6, and Table 2). Note that $\mathbf{FeL^{py}}$ showed no reduction in this range (Fig. 5a and 7), since the $[Fe(NN')_3]^{2+}$ form predominated, avoiding the formation of Fe–H species.

The kinetic isotope effect (KIE = k_H/k_D) was measured by comparing the voltammograms recorded after the addition of the same amount of TFA and d-TFA to $\mathbf{FeL^S}$, as the best performing complex (Fig. S17†). An inverse KIE value was obtained (KIE = 0.64), indicating that the rate-determining step (r.d.s.) of the reaction is somewhat faster when the substrate is deuterated. According to some literature examples, this situation is related to the protonation of a metal–hydride intermediate,[16,78] which involves the formation of [Fe(H–H/D–D)]$^+$ species, during the weakening of Fe–H/D and CF_3CO_2–H/D bonds (Scheme 6). Previous examples for the values of k_H/k_D in the protonation of iron hydrides ranged between 0.21(1) and 0.64(4), depending on the proton source and the iron hydride taking part in the reaction.[79,80] We assume that the reduction of the protonated ligand eventually leads to a metal–hydride intermediate. This is consistent with the observation that the reaction rate significantly decreased when weaker acids were used as the proton source (Fig. S18†).

Taking into account (i) the proton-dependent nature of the first reduction step preceding the onset of catalysis at a more negative potential, altogether setting up a two-electron activation pathway; (ii) the ligand exchange properties of the different complexes; (iii) and lastly, the inverse KIE for $\mathbf{FeL^S}$, two different pathways can be assumed for the formation of hydrogen molecules.[15,16] In a heterolytic reaction mechanism, the protonation of a metal–hydride intermediate is expected to occur, followed by a second reduction (Scheme 6).

This final reduction would allow the rapid elimination of a hydrogen molecule. The last step of the reaction mechanism is the coordination of a ligand (preferably a solvent molecule). Finally, there are precedents where the metal–hydride intermediate may react with another metal–hydride complex, leading to a homolytic reaction mechanism. However, based on the partial order of 1 in complex and 2 in TFA for $\mathbf{FeL^{S/O/NH}}$, a homolytic hydrogen evolution mechanism involving two complex molecules is considered very unlikely.

The thermodynamic viability of the proposed heterolytic mechanism was investigated by DFT calculations. Fig. 8 shows the free energy changes, illustrated with the optimized structures of the proposed intermediates, as appear in Scheme 6 in

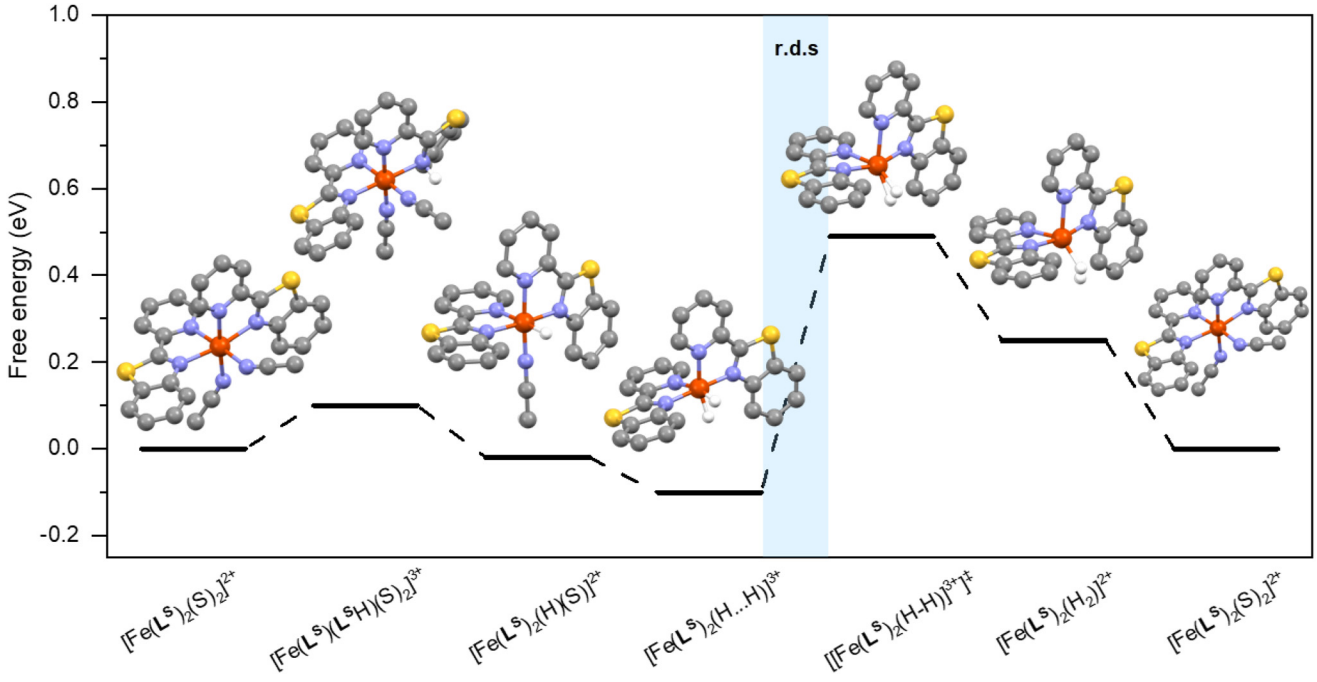

Fig. 8 Free energy diagram of the proposed mechanism (hydrogen atoms of the N,N′ ligands were omitted for clarity).

the case of the most active complex $\mathbf{FeL^S}$. The free energy diagrams for $\mathbf{FeL^O}$ and $\mathbf{FeL^{NH}}$ are presented in Fig. S19.† We chose $[Fe^{II}(NN')_2(S)_2]^{2+}$ as both the start and end point of the cycle to analyze it thermodynamically.

The calculated relative free energies (Table S5†) supported that the transformation of $[Fe^{II}(NN')_2(H\cdots H)]^{2+}$ to $[Fe^{II}(NN')_2(H_2)]^{2+}$ may be rate determining, as it was the most endergonic in all cases. The transition structure of $[Fe^{II}(NN')_2(H–H)]^{2+}$ showed very similar Fe–H (1.794, 1.794, and 1.780 Å for $\mathbf{FeL^S}$, $\mathbf{FeL^O}$, and $\mathbf{FeL^{NH}}$, respectively) and H–H (1.085, 1.081, and 1.081 Å for $\mathbf{FeL^S}$, $\mathbf{FeL^O}$, and $\mathbf{FeL^{NH}}$, respectively) bond distances, indicating the similar energetics of the rate-determining step in all cases (Table S5†). The activation barrier for the r.d.s. were found to be 0.59, 0.57, and 0.62 eV for $\mathbf{FeL^S}$, $\mathbf{FeL^O}$, and $\mathbf{FeL^{NH}}$, respectively. The slight differences indicate a weak electronic effect by the different ligands, which in itself would thus predict only small differences in the activities.

Although the energy barriers of $\mathbf{FeL^O}$, $\mathbf{FeL^S}$, and $\mathbf{FeL^{NH}}$ were close to each other, the impact of tunnelling effects on the penetration coefficient (κ) – especially in such processes involving proton transfer – must be taken into consideration. The κ for $\mathbf{FeL^S}$ $\mathbf{FeL^O}$, and $\mathbf{FeL^{NH}}$ were 0.225, 0.010, and 0.003, respectively, and these differences in κ arose from the different tunnelling distances and tunnelling probabilities of protons after binding to different ligands, suggesting the critical role of the non-coordinating heteroatom of the ligands. Accordingly, the calculated rate constants (k_{DFT}) were 16.45, 1.60, and 0.054 s^{-1} for $\mathbf{FeL^S}$, $\mathbf{FeL^O}$, and $\mathbf{FeL^{NH}}$, respectively (for more details, see ESI†).[81,82] The theoretical results were in excellent agreement with the experimental k_{obs} values (Table 2), supporting the viability of the proposed mechanism for the hydrogen evolution reaction.

Conclusions

In summary, the reactivity of Fe(II) complexes upon reduction in the presence of a proton source can be tuned *via* the non-coordinated heteroatoms of non-symmetrical, bidentate N-heterocyclic ligands. The addition of excess ligands and complex titrations using TFA as an acid showed that the relevant reduction – producing the metal–hydride reactive form – underwent an anodic shift with increasing ligand basicity in the order of $\mathbf{L^S}$, $\mathbf{L^O}$, and $\mathbf{L^{NH}}$. Moreover, the careful design of the ligands allowed influencing the stability of the iron–hydride intermediate. The complex concentration dependence of the excess cathodic current suggested a single-site (heterolytic) mechanism, while the KIE lower than 1 for $\mathbf{FeL^S}$ suggested the protonation of a metal–hydride intermediate involving the formation of $[Fe(H–H/D–D)]^+$ species. Product formation upon controlled potential electrolysis experiments followed the trends in k_{obs} and the rinse tests revealed the homogeneous nature of the studied reaction. The total lowest reactivity, attributed to $[Fe(\mathbf{L^{py}})_3]^{2+}$ – showing no $\mathbf{L^{py}}$ dissociation – suggested that the $[Fe(\mathbf{L^{S/O/NH}})_2(S)_2]^{2+}$ species were the resting form of the cycle, while the $[Fe(\mathbf{L^{S/O/NH}})_3]^{2+}$ species were inactive. The mechanism proposal based on the experimental findings was supported by DFT calculations, and the k_{obs} values for the different complexes clearly showed a strong influence of the non-coordinating heteroatoms in $\mathbf{L^S}$, $\mathbf{L^O}$, and $\mathbf{L^{NH}}$. Our results underline that the design of novel HER catalysts could benefit from heterocyclic sub-structures introduced into metal binding sites of, for example, carbon-based carrier materials, like nanotubes or sheets, and carbon nitrides.

Data availability

Crystallographic data for $\mathbf{FeL^S}$ have been deposited at the Cambridge Crystallographic Data Centre under 2288829.† Other experimental and theoretical data that support the results of this study are available in the main article or in the ESI.†

Conflicts of interest

There are no conflicts of interest to declare.

Acknowledgements

This work was supported by the National Research, Innovation and Development Office of Hungary (Grant Numbers NKFI-128841 and TKP2021-NKTA-05). We also thank the Renewable Energy National Laboratory (Hungary) for support, financed by the RRF-2.3.1-21-2022-00009 project. We are grateful for the microanalysis for Dr Ágnes Szegedi, at the Research Centre for Natural Sciences, Institute of Materials and Environmental Chemistry.

References

1 J. Mitali, S. Dhinakaran and A. A. Mohamad, *Energy Storage Sav.*, 2022, **1**, 166–216.
2 International Energy Agency, Global Hydrogen Review 2023.
3 B. Pivovar, *Nat. Catal.*, 2019, **2**, 562–565.
4 L. Lu, H. Zheng, Y. Li, Y. Zhou and B. Fang, *Chem. Eng. J.*, 2023, **451**, 138668.
5 H.-M. Zhang, J.-J. Wang, Y. Meng and J. Sun, *Int. J. Hydrogen Energy*, 2022, **47**, 36084–36097.
6 L. Zhou, S. Lu and S. Guo, *SusMat*, 2021, **1**, 194–210.
7 F. Abdelghafar, X. Xu, S. P. Jiang and Z. Shao, *Mater. Rep. Energy*, 2022, **2**, 100144.
8 V. S. Thoi, Y. Sun, J. R. Long and C. J. Chang, *Chem. Soc. Rev.*, 2013, **42**, 2388–2400.
9 K. E. Dalle, J. Warnan, J. J. Leung, B. Reuillard, I. S. Karmel and E. Reisner, *Chem. Rev.*, 2019, **119**, 2752–2875.
10 L. Tong, L. Duan, A. Zhou and R. P. Thummel, *Coord. Chem. Rev.*, 2020, **402**, 213079.

11 D. L. DuBois, *Inorg. Chem.*, 2014, **53**, 3935–3960.
12 V. Artero, M. Chavarot-Kerlidou and M. Fontecave, *Angew. Chem., Int. Ed.*, 2011, **50**, 7238–7266.
13 J. R. McKone, S. C. Marinescu, B. S. Brunschwig, J. R. Winkler and H. B. Gray, *Chem. Sci.*, 2014, **5**, 865–878.
14 W. Lubitz, H. Ogata, O. Rüdiger and E. Reijerse, *Chem. Rev.*, 2014, **114**, 4081–4148.
15 G.-G. Luo, H.-L. Zhang, Y.-W. Tao, Q.-Y. Wu, D. Tian and Q. Zhang, *Inorg. Chem. Front.*, 2019, **6**, 343–354.
16 M. Drosou, F. Kamatsos and C. A. Mitsopoulou, *Inorg. Chem. Front.*, 2020, **7**, 37–71.
17 S. Shima, O. Pilak, S. Vogt, M. Schick, M. S. Stagni, W. Meyer-Klaucke, E. Warkentin, R. K. Thauer and U. Ermler, *Science*, 2008, **321**, 572–575.
18 F. Gloaguen, J. D. Lawrence and T. B. Rauchfuss, *J. Am. Chem. Soc.*, 2001, **123**, 9476–9477.
19 S. Ott, M. Kritikos, B. Åkermark, L. Sun and R. Lomoth, *Angew. Chem., Int. Ed.*, 2004, **43**, 1006–1009.
20 L. Duan, M. Wang, P. Li, Y. Na, N. Wang and L. Sun, *Dalton Trans.*, 2007, 1277–1283.
21 B. E. Barton and T. B. Rauchfuss, *Inorg. Chem.*, 2008, **47**, 2261–2263.
22 M. E. Carroll, B. E. Barton, T. B. Rauchfuss and P. J. Carroll, *J. Am. Chem. Soc.*, 2012, **134**, 18843–18852.
23 Y. Na, M. Wang, K. Jin, R. Zhang and L. Sun, *J. Organomet. Chem.*, 2006, **691**, 5045–5051.
24 U. Apfel, Y. Halpin, M. Gottschaldt, H. Görls, J. G. Vos and W. Weigand, *Eur. J. Inorg. Chem.*, 2008, **2008**, 5112–5118.
25 L.-C. Song, L. Feng and Y.-Q. Guo, *Dalton Trans.*, 2019, **48**, 1443–1453.
26 W.-N. Cao, F. Wang, H.-Y. Wang, B. Chen, K. Feng, C.-H. Tung and L.-Z. Wu, *Chem. Commun.*, 2012, **48**, 8081.
27 J.-X. Jian, C. Ye, X.-Z. Wang, M. Wen, Z.-J. Li, X.-B. Li, B. Chen, C.-H. Tung and L.-Z. Wu, *Energy Environ. Sci.*, 2016, **9**, 2083–2089.
28 M. L. Singleton, D. J. Crouthers, R. P. Duttweiler, J. H. Reibenspies and M. Y. Darensbourg, *Inorg. Chem.*, 2011, **50**, 5015–5026.
29 M. Cheng, M. Wang, S. Zhang, F. Liu, Y. Yang, B. Wan and L. Sun, *Faraday Discuss.*, 2017, **198**, 197–209.
30 A. Onoda, Y. Kihara, K. Fukumoto, Y. Sano and T. Hayashi, *ACS Catal.*, 2014, **4**, 2645–2648.
31 F. Quentel, G. Passard and F. Gloaguen, *Chem. – Eur. J.*, 2012, **18**, 13473–13479.
32 F. Quentel, G. Passard and F. Gloaguen, *Energy Environ. Sci.*, 2012, **5**, 7757.
33 A. Begum and S. Sarkar, *Eur. J. Inorg. Chem.*, 2012, **2012**, 40–43.
34 S. Ezzaher, A. Gogoll, C. Bruhn and S. Ott, *Chem. Commun.*, 2010, **46**, 5775.
35 I. Bhugun, D. Lexa and J.-M. Savéant, *J. Am. Chem. Soc.*, 1996, **118**, 3982–3983.
36 D. J. Graham and D. G. Nocera, *Organometallics*, 2014, **33**, 4994–5001.
37 X. Qi, G. Yang, X. Guo, L. Si, H. Zhang and H. Liu, *Eur. J. Inorg. Chem.*, 2023, **26**, e202200613.
38 Y.-Q. Zhong, Md. S. Hossain, Y. Chen, Q.-H. Fan, S.-Z. Zhan and H.-Y. Liu, *Transition Met. Chem.*, 2019, **44**, 399–406.
39 L.-W. Wu, Y.-F. Yao, S.-Y. Xu, X.-Y. Cao, Y.-W. Ren, L.-P. Si and H.-Y. Liu, *Catalysts*, 2023, **14**, 5.
40 W.-Y. Peng, J. Lan, Z.-M. Zhu, L.-P. Si, H. Zhang, S.-Z. Zhan and H.-Y. Liu, *Inorg. Chem. Commun.*, 2022, **140**, 109453.
41 S.-P. Luo, Q.-X. Peng, J. Liu and S.-Z. Zhan, *Polyhedron*, 2018, **139**, 44–49.
42 A. V. Dolganov, A. V. Dolganov, A. V. Dolganov, O. V. Tarasova, O. V. Tarasova, A. Y. Ivleva, A. Y. Ivleva, O. Y. Chernyaeva, O. Y. Chernyaeva, K. A. Grigoryan, K. A. Grigor'yan, V. S. Ganz and V. S. Ganz, *Int. J. Hydrogen Energy*, 2017, **42**, 27084–27093.
43 A. C. Cavell, C. L. Hartley, D. Liu, C. S. Tribble and W. R. McNamara, *Inorg. Chem.*, 2015, **54**, 3325–3330.
44 G. P. Connor, K. J. Mayer, C. S. Tribble and W. R. McNamara, *Inorg. Chem.*, 2014, **53**, 5408–5410.
45 C. L. Hartley, R. J. DiRisio, M. E. Screen, K. J. Mayer and W. R. McNamara, *Inorg. Chem.*, 2016, **55**, 8865–8870.
46 M. Tagliapietra, A. Squarcina, N. Hickey, R. De Zorzi, S. Geremia, A. Sartorel and M. Bonchio, *ChemSusChem*, 2017, **10**, 4430–4435.
47 C. L. Hartley, R. J. DiRisio, T. Y. Chang, W. Zhang and W. R. McNamara, *Polyhedron*, 2016, **114**, 133–137.
48 H. C. Hernández-Toledo, M. Flores-Alamo and I. Castillo, *J. Inorg. Biochem.*, 2023, **241**, 112128.
49 J. S. Pap, A. Draksharapu, M. Giorgi, W. R. Browne, J. Kaizer and G. Speier, *Chem. Commun.*, 2014, **50**, 1326–1329.
50 S. M. Al-Zuraiji, T. Benkó, L. Illés, M. Németh, K. Frey, A. Sulyok and J. S. Pap, *J. Catal.*, 2020, **381**, 615–625.
51 H.-L. Xia, S. Ardo, A. A. Narducci Sarjeant, S. Huang and G. J. Meyer, *Langmuir*, 2009, **25**, 13641–13652.
52 C. T. Lin, W. Boettcher, M. Chou, C. Creutz and N. Sutin, *J. Am. Chem. Soc.*, 1976, **98**, 6536–6544.
53 *CrysAlisPRO Oxford Diffraction*, Agilent Technologies UK Ltd, Yarnton, England.
54 G. M. Sheldrick, *Acta Crystallogr., Sect. A: Found. Crystallogr.*, 2008, **64**, 112–122.
55 S. J. Clark, M. D. Segall, C. J. Pickard, P. J. Hasnip, M. I. J. Probert, K. Refson and M. C. Payne, *Z. Kristallogr. – Cryst. Mater.*, 2005, **220**, 567–570.
56 J. P. Perdew, K. Burke and M. Ernzerhof, *Phys. Rev. Lett.*, 1996, **77**, 3865–3868.
57 D. Vanderbilt, *Phys. Rev. B: Condens. Matter Mater. Phys.*, 1990, **41**, 7892–7895.
58 A. Tkatchenko and M. Scheffler, *Phys. Rev. Lett.*, 2009, **102**, 073005.
59 B. Cordero, V. Gómez, A. E. Platero-Prats, M. Revés, J. Echeverría, E. Cremades, F. Barragán and S. Alvarez, *Dalton Trans.*, 2008, 2832.
60 J. R. Sams and T. B. Tsin, *J. Chem. Soc., Dalton Trans.*, 1976, 488–496.
61 J. R. Sams and T. B. Tsin, *Inorg. Chem.*, 1976, **15**, 1544–1550.

62 Z. Setifi, F. Setifi, H. Boughzala, A. Beghidja and C. Glidewell, *Acta Crystallogr., Sect. C: Struct. Chem.*, 2014, **70**, 465–469.
63 C. Duboc-Toia, S. Ménage, R. Y. N. Ho, L. Que, C. Lambeaux and M. Fontecave, *Inorg. Chem.*, 1999, **38**, 1261–1268.
64 M. Wang, H. Sun, Y. Wang, X. Wang, F. Li and L. Sun, *Appl. Organomet. Chem.*, 2004, **18**, 277–281.
65 M. I. Szávuly, M. Surducan, E. Nagy, M. Surányi, G. Speier, R. Silaghi-Dumitrescu and J. Kaizer, *Dalton Trans.*, 2016, **45**, 14709–14718.
66 D. Lakk-Bogáth, P. Török, F. V. Csendes, S. Keszei, B. Gantner and J. Kaizer, *Molecules*, 2021, **26**, 4501.
67 P. Török, D. Unjaroen, F. V. Csendes, M. Giorgi, W. R. Browne and J. Kaizer, *Dalton Trans.*, 2021, **50**, 7181–7185.
68 W. J. Geary, *Coord. Chem. Rev.*, 1971, **7**, 81–122.
69 M. Irwin, R. K. Jenkins, M. S. Denning, T. Krämer, F. Grandjean, G. J. Long, R. Herchel, J. E. McGrady and J. M. Goicoechea, *Inorg. Chem.*, 2010, **49**, 6160–6171.
70 M. Irwin, L. R. Doyle, T. Krämer, R. Herchel, J. E. McGrady and J. M. Goicoechea, *Inorg. Chem.*, 2012, **51**, 12301–12312.
71 H. M. Hüppe, L. Iffland-Mühlhaus, J. Heck, M. Eilers, H. Gildenast, S. Schönfeld, A. Dürrmann, A. Hoffmann, B. Weber, U.-P. Apfel and S. Herres-Pawlis, *Inorg. Chem.*, 2023, **62**, 4435–4455.
72 F. G. Bordwell, *Acc. Chem. Res.*, 1988, **21**, 456–463.
73 B. D. McCarthy, D. J. Martin, E. S. Rountree, A. C. Ullman and J. L. Dempsey, *Inorg. Chem.*, 2014, **53**, 8350–8361.
74 J. Brown, J. Ovens and D. Richeson, *ChemSusChem*, 2022, **15**, e202102542.
75 V. Fourmond, P.-A. Jacques, M. Fontecave and V. Artero, *Inorg. Chem.*, 2010, **49**, 10338–10347.
76 K. J. Lee, N. Elgrishi, B. Kandemir and J. L. Dempsey, *Nat. Rev. Chem.*, 2017, **1**, 0039.
77 E. S. Rountree, B. D. McCarthy, T. T. Eisenhart and J. L. Dempsey, *Inorg. Chem.*, 2014, **53**, 9983–10002.
78 M. Gómez-Gallego and M. A. Sierra, *Chem. Rev.*, 2011, **111**, 4857–4963.
79 M. G. Basallote, J. Durán, M. J. Fernández-Trujillo and M. A. Máñez, *J. Chem. Soc., Dalton Trans.*, 1998, 2205–2210.
80 M. G. Basallote, J. Durán, M. J. Fernández-Trujillo, M. A. Máñez and J. Rodríguez De La Torre, *J. Chem. Soc., Dalton Trans.*, 1998, 745–750.
81 R. P. Bell, *The tunnel effect in chemistry*, Chapman and Hall, London, New York, 1980.
82 L. I. Krishtalik, *Electrochim. Acta*, 2001, **46**, 2949–2960.